

PBO fiber grafted rGO aerogel/BN/PBO composites with highly improved electromagnetic interference shielding effectiveness and through-plane thermal conductivity

Jihoon Kim^a, Jooheon Kim^{a,b,c,*}

^a School of Chemical Engineering & Materials Science, Chung-Ang University, 84 Heukseok-ro, Dongjak-gu, Seoul, Republic of Korea

^b Department of Advanced Materials Engineering, Chung-Ang University, Anseong-si, Gyeonggi-do, 17546, Republic of Korea

^c Department of Intelligent Energy and Industry, Graduate School, Chung-Ang University, Seoul, 06974, Republic of Korea

ARTICLE INFO

Keywords:

Thermal conductivity
Electromagnetic interference shielding effectiveness
PBO fiber grafting
Reduced graphene oxide aerogel

ABSTRACT

With the advancement of electronic devices, the generation of heat and electromagnetic (EM) waves has increased. Therefore, it is essential to properly manage these heat and EM waves, while ensuring the flame retardancy and mechanical properties of the materials used in these devices. In this study, to compensate for the low thermal and electrical conductivity of Poly(*p*-phenylene-2,6-benzobisoxazole) (PBO), which was used as the matrix, reduced graphene oxide aerogel (rGOA) with high electrical conductivity and electromagnetic interference shielding effectiveness (EMI SE) performance and boron nitride (BN) with high thermal conductivity were selected as fillers (rGOA/BN). To significantly improve the compatibility of the filler with the matrix, PBO fiber was grafted onto the rGOA/BN filler. The fabricated composites exhibited high electrical conductivity of 21.1 S/cm and thermal conductivity of 4.81 W/m•K, and the EMI SE and tensile strength were improved to up to 78.42 dB and 201.8 MPa, respectively.

1. Introduction

As electronic devices have progressed, there has been an escalation in the generation of heat from these devices. Failure to manage this generated heat will adversely affect electronic devices [1,2]. Therefore, it is necessary to ensure the proper dissipation of this generated heat [3–6]. In addition, electromagnetic interference (EMI) caused by external electromagnetic (EM) waves in electronic devices should be considered because it causes problems in the operation of electronic devices and harms humans [7–11]. In electronic devices, these EM waves are converted into thermal energy as they are reflected or absorbed [12–14]. Therefore, EMI shielding effectiveness (SE) must be considered for the effective management of heat in electronic devices [15–17]. In addition, materials used in electronic devices should exhibit flame retardancy and fire resistance properties as the poor management of heat results in the accumulation of heat inside the devices, which can lead to fire accidents. With the increasing number of fire accidents in electronic devices, it is essential to ensure that these devices exhibit flame retardancy [18].

Polymer-based materials are widely used to produce multifunctional

composites with these properties. Owing to their affordability, light-weight nature, resistance to corrosion, and ease of processing, polymers find application in various fields [19–28]. On the other hand, they exhibit poor heat dissipation performance and EMI SE owing to their low thermal and electrical conductivity. To compensate for this, the fabrication of polymer composites by introducing fillers with high thermal conductivity has been proposed. These fillers include boron nitride (BN) [29–33], alumina [34–38], aluminum nitride [39–41], graphene [42–44], and carbon nanotube [45–47]. Among these fillers, BN is a two-dimensional (2D) material with a high aspect ratio. In addition, it exhibits advantages, such as low dielectric constant and high resistance to corrosion [48]. In addition, the properties of reduced graphene oxide (rGO) include high thermal conductivity, a low thermal expansion coefficient, excellent mechanical properties, affordability, and low density [49]. Furthermore, rGO aerogel (rGOA) exhibits a three-dimensional (3D) structure and high flexibility, oxidation stability, mechanical strength, and electrical conductivity. Particularly, Graphene aerogel exhibits high flame resistance and excellent self-extinguishing behavior [50]. Upon exposure to flames, rGOA acts as a physical protective layer that interferes with heat transfer and delays the release of combustible

* Corresponding author. School of Chemical Engineering & Materials Science, Chung-Ang University, 84 Heukseok-ro, Dongjak-gu, Seoul, Republic of Korea.
E-mail address: jooheonkim@cau.ac.kr (J. Kim).

gases by forming a char layer on the surface. In addition, it inhibits combustion reactions by blocking the injection of oxygen gas. However, rGOA exhibits a low thermal conductivity [51], making it unsuitable for use as a thermally conductive filler.

In this study, a rGOA/BN hybrid filler was fabricated to achieve the combined excellent properties of rGOA and the high thermal conductivity of BN. As an aerogel, rGOA exhibits a porous structure, and BN nanosheets (BNNS) were introduced into these pores to form a heat transfer path. Both rGOA and BN exhibit high thermal stability and excellent flame retardancy, indicating their suitability as fillers for composites. Owing to its remarkable fire resistance, thermal stability, and superior mechanical properties, a polymer known as poly(*p*-phenylene-2,6-benzobisoxazole) (PBO) was selected as the matrix of the composite [52]. Owing to its excellent properties, PBO has been used in various composite materials [53–55]. The interfacial compatibility between the matrix and the filler has a substantial impact on the performance of composites. In this study, PBO fibers were grafted on the surface of rGOA to enhance the interfacial compatibility between the rGOA/BN hybrid filler and the PBO matrix. The PBO fibers grafting was performed using the solvothermal process [56]. The rGOA/BN filler grafted with PBO fibers (PrGOA/BN) exhibited high interfacial compatibility with the PBO matrix. Owing to the high electrical conductivity and 3D porous structure of rGOA, the composite exhibited excellent EMI SE performance. In addition, owing to the exceptional flame resistance of BN, rGOA, and PBO, the composites exhibited flame resistance properties.

A composite with high thermal conductivity and electrical conductivity was fabricated to simultaneously achieve thermal management and EM wave shielding. It is expected that fire accidents can be prevented when flame-resistance materials are used in composites. In

addition to the high mechanical properties of rGOA and BN, the grafting of the PBO fiber also enhanced the mechanical characteristics of the composite material. Because of these exceptional characteristics, the fabricated composite is expected to be used in industries that require composites that exhibit both heat dissipation performance and EMI shielding effects.

2. Experimental

2.1. Materials

The PBO fibers were supplied by Toyobo Co. Ltd. (Japan). Graphene oxide powder was supplied by Grapheneall (Korea). Hexagonal BN powder was provided by Momentive Performance Materials Inc (USA). Ethylenediamine (EDA, 99%) was purchased from Sigma Aldrich (Korea). Trifluoroacetic acid (TFA, 99%), Methane sulfonic acid (MSA, 99%), *N,N*-dimethylformamide (99.5%), Tetrahydrofuran (99.5%), and Hydroiodic acid (HI, 55%) were supplied by Daejung Chemicals (Korea).

2.2. Preparation of rGOA/BNNS hybrid filler

Fig. 1 shows all stages of the experiment. To prepare the rGOA/BNNS hybrid filler, graphene oxide was placed in deionized (DI) water, and subjected to ultrasonication for 1 h. In addition, GO was converted into rGO hydrogel through a hydrothermal process at 180 °C for 12 h. Thereafter, the rGO hydrogel was subjected to vacuum filtration, after which it was freeze-dried. Subsequently, rGO aerogel (rGOA) with a porous structure was formed. The h-BN was dispersed in an isopropyl alcohol (IPA) solvent using ultrasonication. Subsequently, h-BN was exfoliated to BNNS through a ball milling process. The as-prepared

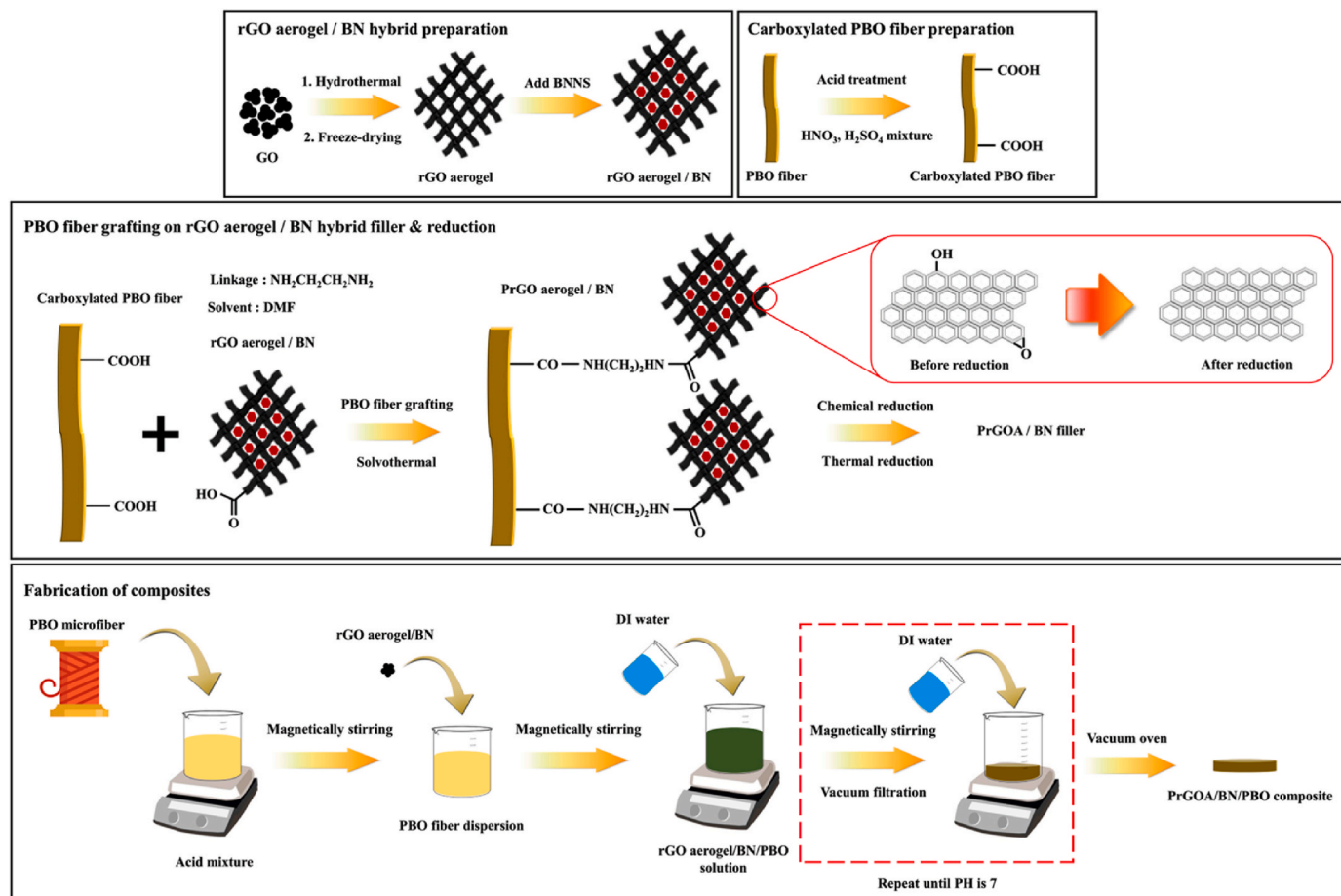


Fig. 1. Schematic illustration of the composites fabrication process.

BNNS and rGOA were evenly dispersed in an IPA solvent through bath sonication during which the BNNS was inserted into the rGOA pores. Solvent exchange of this rGOA/BNNS hybrid filler and IPA mixture to N, N-dimethylformamide (DMF) was performed.

2.3. PBO fiber grafting process

To graft the PBO fibers, the PBO microfiber was subjected to magnetic stirring at room temperature in a mixture of MSA and TFA (volume ratio 1:1) for 5 days. The preparation of the PBO fiber solution was completed when the solution turned yellow with a high viscosity. Thereafter, a mixture of sulfuric acid and nitric acid (volume ratio 3:2) was used to introduce carboxyl groups onto the PBO fiber (PBO-COOH). Subsequently, the PBO fiber was immersed and magnetically stirred in an acid mixture at 75 °C for 24 h. Thereafter, the oxidized PBO fiber powder was obtained through vacuum filtration. The PBO-COOH powder and rGOA/BNNS were dispersed in DMF through bath sonication. Subsequently, EDA was added to connect PBO-COOH and rGOA. The mixture was poured into a Teflon-lined autoclave and heated at 180 °C for 24 h, after which it was cooled to room temperature. EDA chemically forms a bond between PBO-COOH and rGOA through the dehydration reaction. Thereafter, vacuum filtration was performed, and excess tetrahydrofuran (THF) was added to the mixture to remove the remaining DMF and EDA. After vacuum filtration, the obtained sample was dried in a vacuum oven at 80 °C for 24 h. The sample was immersed in the HI solution, it was chemically reduced and then taken out. Lastly, the thermal reduction was performed at 600 °C for 6 h.

2.4. Fabrication of composites

To fabricate the composite, the filler was dissolved in the PBO-dispersed MSA and TFA mixture. The mixture was mixed under magnetic stirring until the filler was dispersed. The mixture was transferred to a petri dish and the mixture was allowed to stand for 24 h for gelation. Thereafter, DI water was added to the mixture until a DI water content of 70 vol%. After vacuum filtration, the solvent was changed to DI water, and the mixture was magnetically stirred. This process was repeated until the pH of the solution after vacuum filtration reached 7. The prepared composite was dried in a vacuum oven at 80 °C for 24 h.

2.5. Characterization

The chemical structures analysis was performed using Fourier transform infrared (FT-IR) spectroscopy (ATR mode, Perkin-Elmer, Spectrum One) and X-ray photoelectron spectroscopy (XPS, VGMicrotech). The crystalline structures of the filler and matrix were examined using X-ray diffraction (XRD, Bruker-AXS, D8-Advance) at a scan rate of 0.2° s⁻¹ with Cu K α radiation (0.154056 nm) in a 2 θ range of 10–80°. The morphologies were confirmed using field-emission scanning electron microscopy (FE-SEM, Carl Zeiss, Sigma). Energy-dispersive X-ray spectroscopy (EDS) was operated at 30 kV using the Thermo NORAN System 7 to investigate the atomic composition of the fillers. The thermal stability was investigated using thermogravimetric analysis (TGA, TGA-2050, TA Instruments). The TGA was conducted by heating the samples to 800 °C at a heating rate of 10 °C min⁻¹ under a nitrogen atmosphere. The thermal diffusivities of the composites at room temperature were determined using laser flash analysis (LFA, Netzsch Instruments Co., NanoFlash LFA 467). The thermal conductivities were calculated using $K = \alpha \times \rho \times C_p$, where K is the thermal conductivity (W/m•K), α is the thermal diffusivity (mm²/s), ρ is the bulk density (g/cm³), and C_p is the room-temperature heat capacity (J/g•K). The electrical conductivities were calculated using the four-point probe method. The EMI SE values were examined using equations (1)–(4):

$$R = |S_{11}|^2 = |S_{22}|^2, T = |S_{12}|^2 = |S_{21}|^2 \quad (1)$$

$$SE_R = 10 \log \left(\frac{1}{1 - |S_{11}|^2} \right) \quad (2)$$

$$SE_A = 10 \log \left(\frac{1 - |S_{11}|^2}{|S_{21}|^2} \right) \quad (3)$$

$$SE_T = SE_R + SE_A + SE_M \quad (4)$$

Where R is the reflective power, T is the transmittive power, SE_R , SE_A , SE_M and SE_T are the reflective, absorptive, multiple-reflective, and total EMI SE, respectively. S_{11} , S_{12} , S_{21} , S_{22} are the parameters calculated using a network analyzer (E8364B) in the range of 8.2 and 12.4 GHz (X-band). The SE_M can be ignored when $SE_T \geq 15$ dB. For these measurements, toroidal-shaped composite specimens ($\phi_{out} = 12.0$ mm, $\phi_{in} = 2.4$ mm, and $t = 0.5$ mm) were fabricated. The tensile strengths were investigated using a universal testing machine (UTM; model UTM-301, R&B Corp., Daejeon, Korea) at room temperature at a crosshead speed of 5 mm/min, tension loading rate of 10 mm/min, and load force of 100 Kg forces/mm. To investigate the fire retardancy of the composites, the limited oxygen index (LOI) was obtained on an oxygen index meter (LOI-404) according to ASTM D 2863. The flammability of the composites was measured in Underwriters Laboratory (UL94-V), by directly applying a flame to composite samples (40 × 10 × 3 mm³) for a certain time.

3. Results and discussion

3.1. Composites fabrication process

Fig. 1 illustrates the preparation process of fillers and composites. Detailed procedures can be found in the experimental section.

3.2. Characterization of fillers

Fig. 2 exhibits the morphologies of fillers. The FESEM image of the as-prepared rGOA indicated that it exhibited a porous structure (Fig. 2(a)). When GO was freeze-dried after undergoing a hydrothermal process, it exhibited an aerogel structure. The sizes of the pores ranged from 1 to 5 μm . Compared to the following research, 3D cellular rGOA was well formed [50]. The morphology of rGOA/BN filler fabricated by inserting BNNS particles into rGOA is shown in Fig. 2(b). The sizes of the BNNSs ranged from 1 to 3 μm , and the BNNSs fitted inside the pores. The good penetration of the BNNS in the pores of the rGOA confirmed the success of the procedure. In addition, no agglomeration of BNNSs was observed. The morphology of the raw GO-BN in Fig. 2(c) confirmed the random dispersion of the BNNSs. The compatibility of hydrophilic GO, which consisted of numerous oxygen functional groups on its surface, and hydrophobic BN was poor compared to that of rGOA/BN. Compared to rGOA, GO does not exhibit a porous structure and was simply mixed with BNNSs. Consequently, GO flakes and BNNSs were located at separate locations. Each filler in the raw GO-BN agglomerated according to its type, as shown in Fig. S1. The SEM image of the pure PBO fiber indicated that it exhibited a smooth surface (Fig. 2(d)). In addition, carboxyl groups were attached to the acid-treated PBO (PBO-COOH) (Fig. 2(e)). After oxidation in the strong acid mixture, the smooth surface of the PBO changed to a rough surface. Fig. 2(f) shows an image of the PrGOA/BN hybrid filler. Compared to Fig. 2(d), changes are evident on the surface of the PBO fiber. The appearance of the PBO fiber attached to rGOA confirmed the successful grafting process. EDA was used to chemically link PBO-COOH with rGOA. PBO fiber was grafted only to rGOA, while BNNSs were physically inserted into the pores of rGOA. The magnified image (Fig. 2(g)) confirmed that the BNNSs were well-settled in the rGOA pores. The grafting of PBO fiber was confirmed through various other analytical methods (FT-IR, XPS, XRD, TGA).

The functional groups of fillers were analyzed using FTIR. Peaks

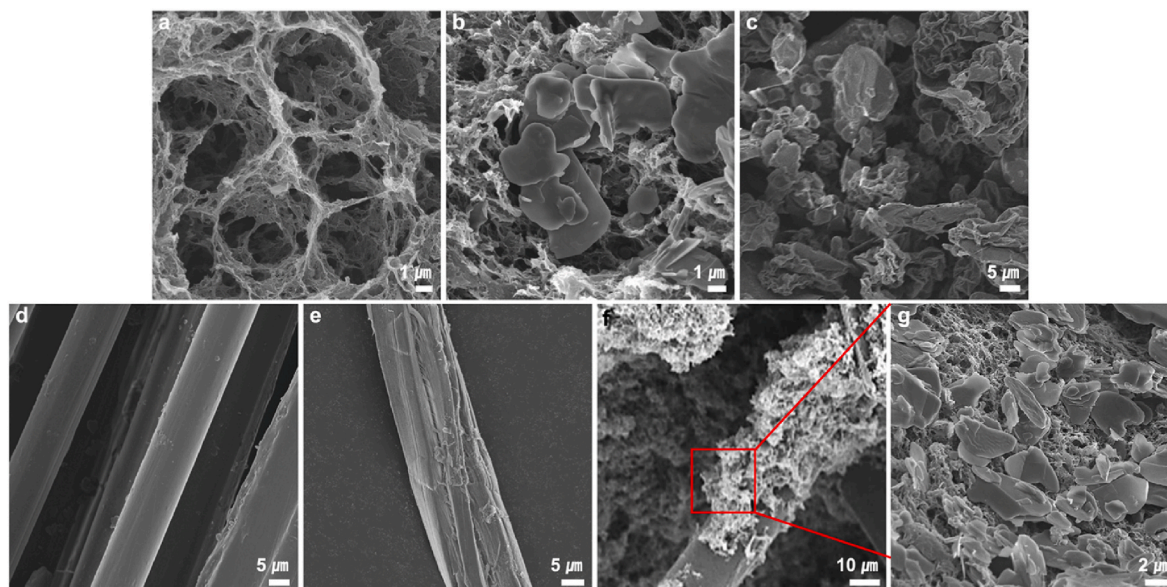


Fig. 2. FE-SEM images of (a) rGOA, (b) rGOA/BN, (c) raw GO-BN, (d) PBO fiber, (e) acid-treated PBO fiber, (f) PrGOA/BN, and (g) magnified PrGOA/BN.

corresponding to C–O–C (1056 cm^{-1}) and C=O (1734 cm^{-1}) stretching vibration and unoxidized C=C sp^2 aromatic ring bands (1615 cm^{-1}) were observed in the raw GO (Fig. 3(a)). The broad peak observed at 3400 cm^{-1} corresponds to the O–H stretching vibration. Peaks were observed at 1371 (B–N stretching vibration) and 827 cm^{-1} (B–N–B out-of-plane bending) in the FTIR spectrum of the raw BN. The peaks of raw BN and raw GO (O–H, C=O, C=C, B–N, C–O–C, and B–N–B) were observed in the FTIR spectrum of the raw GO-BN. Fig. 3(b) shows the FTIR spectra of the rGOA/BN and PrGOA/BN. The peaks of BN (B–N and B–N–B) were maintained in the FTIR spectra of rGOA/BN, whereas most of the peaks of GO disappeared. This can be attributed to the decomposition of most of the oxygen functional groups during the reduction process. Except for peaks of BN, C=O (1758 cm^{-1}) and C=C (1640 cm^{-1}) functional groups were observed. The following functional groups were observed in the FTIR spectrum of the pure PBO: aromatic C–H stretch (3018 cm^{-1}), C–O–C (1059 cm^{-1}), and C–N stretch (1630 cm^{-1}). The FTIR analysis of the intermediate process of grafting the PBO fiber is shown in Fig. S2. Peaks of PBO fibers (C–H, C–O–C, C–N) and peaks of rGOA/BN were observed in PrGOA/BN, in which PBO fibers were grafted on rGOA/BN. Fig. 3(c) shows the XPS profiles to further confirm the grafting of the PBO fiber. Peaks of C–C (284.4 eV), C–N (286.5 eV), N=C–O (287.7 eV), and N–C=O (289.1 eV) were observed in the C1s spectra of PrGOA/BN. The XPS C1s spectra of raw GO-BN and rGOA/BN fillers are in Fig. S3. Unlike PrGOA/BN filler, peaks corresponding to C–N, N=C–O, and N–C=O were not observed in raw GO-BN and rGOA/BN. This difference is attributed to the grafting process. The XPS C1s spectra for the intermediate process of grafting the PBO fiber to GO are shown in Fig. S4. Most of the peaks observed were peaks for PBO fibers; however, new N–C=O peaks appeared, which can be attributed to the transformation of the carboxyl groups into an amide group as EDA was linked between the carboxyl group of rGOA and PBO-COOH. The generation of the N–C=O functional group indicates that the grafting of the PBO fiber progressed smoothly. Owing to the reduction, the peaks of the oxygen functional groups disappeared compared to those of PBO and PBO-COOH, which are shown in Fig. S3. Fig. 3(d) represents the XPS survey scan spectra of PrGOA/BN. The peaks of O1s (532.9 eV), N1s (394.2 eV), C1s (283.5 eV), and B1s (181.7 eV) were observed. We analyzed the elemental composition using EDS. The contents of oxygen, nitrogen, carbon, and boron were 12.74, 18.53, 55.64, and 13.09%, respectively. The presence of the B1s peak and the content indicated the presence of BN in PrGOA/BN. Survey scan spectra of PBO, PBO-COOH,

and PBO-GO are shown in Fig. S5.

Fig. 4(a) shows XRD patterns of the fillers. Peaks of GO were observed in the raw GO-BN at 10.3 and 26.2° , corresponding to the (001) and (002) planes, respectively. In addition, the peaks of BN were observed in the raw GO-BN at 26.7 , 41.3 , 43.7 , 50.1 , 55.3 , and 76.8° , corresponding to the (002), (100), (101), (102), (004), and (110) planes, respectively. The peaks corresponding to the (001) plane of GO were lost in the XRD pattern of rGOA/BN. The peaks of the (002) plane of GO and BN merged into one peak at 26.4° . All the peaks of BN except the peaks corresponding to the (002) plane were maintained. In addition, new peaks attributed to PBO fiber were observed in the XRD pattern of PrGOA/BN. Peaks corresponding to (200) and (010) plane appeared at 16.1 and 25.9° , confirming the successful grafting of the PBO fiber. There was no change in the BN peaks, but there was a slight shift in the peaks corresponding to the (002) plane of rGOA/BN, indicating the slight effect of the PBO fiber grafting on the crystallinity of rGOA/BN. Fig. 4(b) demonstrates the TGA graphs of the fillers. The raw GO-BN exhibited the most significant mass loss among the fillers after heating to 800°C owing to the decomposition of GO. The mass of the raw BN reduced slightly, whereas that of raw GO reduced significantly (Fig. S6), which can be attributed to the decomposition of most of the oxygen functional groups in GO, leading to a large mass loss. The final mass of the residue of the raw GO-BN was 53.07%, whereas there was no reduction in the mass of rGOA/BN. This can be attributed to the fact that rGOA contained few oxygen functional groups after reduction, so there were no functional groups to decompose, and to the high thermal stability of raw BN. In contrast, the mass of the rGOA/BN increased and reached 102.18%. This is because of the adsorption of gas molecules into the pores of rGOA owing to the large surface area and porous structure of rGOA [50]. The PrGOA/BN exhibited a 14.65% mass reduction owing to the grafting of the PBO fiber. At temperatures below 600°C , there was a slight mass reduction, which became significant from 650°C , which is consistent with the TGA results of PBO [57]. In addition, the mass of PrGOA/BN increased as gas molecules entered the rGOA pores, but the decomposition effect of PBO fibers was greater, so there was no increase in mass. These TGA results confirmed the successful grafting of the PBO fiber.

3.3. Morphology of the composites

Fig. 5 shows the cross-sectional images of the PBO matrix and

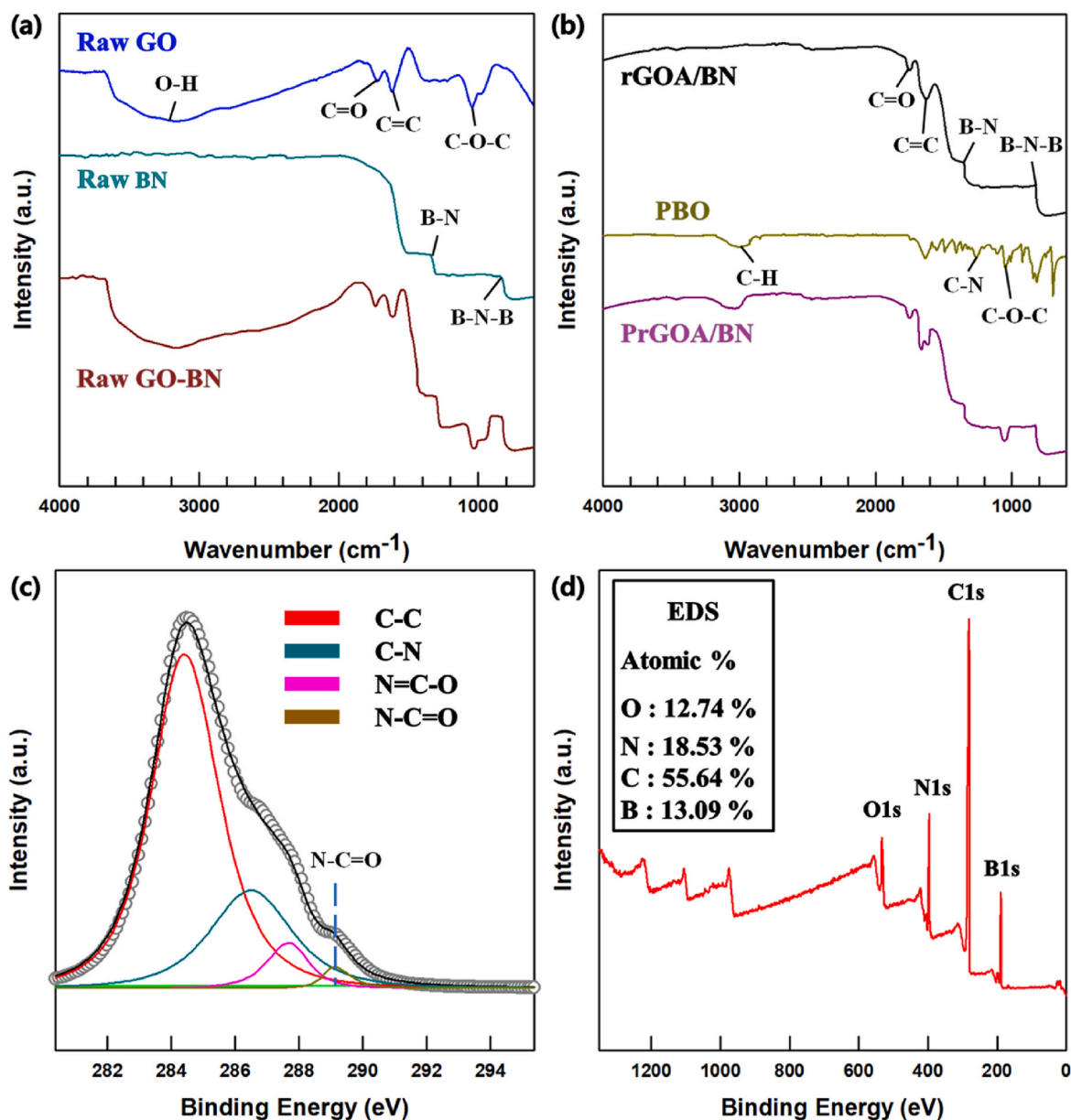


Fig. 3. FTIR of (a) raw GO-BN and (b) FTIR of rGOA/BN and PrGOA/BN. (c) XPS C1s spectra of PrGOA/BN, and (d) survey scan of PrGOA/BN (Inset is EDS measurement result).

composites. The image indicated that the PBO matrix exhibited a smooth surface (Fig. 5(a)). In contrast, the raw GO-BN/PBO composite exhibited a very rough surface (Fig. 5(b)). In addition, GO and BN were randomly mixed in the composite, and the surface was uneven. This was attributed to the poor compatibility of raw GO-BN, which resulted in poor dispersion in the PBO matrix. Furthermore, several empty spaces were observed in the raw GO-BN/PBO composite even though it did not have an aerogel structure or was subjected to freeze-drying. Owing to the low interfacial compatibility between the filler and the matrix, randomly-sized voids were detected in this composite. Compared to the raw GO-BN/PBO composite, the rGOA/BN/PBO composite exhibited an even surface (Fig. 5(c)). Compared to GO, rGOA exhibits significantly reduced hydrophilicity owing to the significant removal of oxygen functional groups. In addition, owing to the hydrothermal and freeze-drying processes, the rGOA exhibited a porous structure, enabling the entry of BNNSs into the pores. The rGOA/BN/PBO composite contained numerous pores owing to the porous structure of rGOA. Because of the improved compatibility of the rGOA/BN filler, the rGOA/BN/PBO

composite exhibited more aligned surface than the raw GO-BN/PBO composite. Fig. 5(d) shows an image of the PrGOA/BN/PBO composite. The interfacial compatibility of the composite was significantly improved, showing the most even surface among the composites. As the filler exhibited a porous structure, some pores were observed in the PrGOA/BN/PBO compared to pure PBO fibers. In addition, BNNS was observed on the surface of the rGOA/BN/PBO, whereas BNNS was rarely observed on the surface of PrGOA/BN/PBO. The grafting of the PBO fiber significantly improved the dispersibility of rGOA, and the distribution of pores became uniform, enabling the uniform entry of BNNSs into the pores. As some pores were covered by the PBO fiber, fewer pores were observed in the PrGOA/BN/PBO composite than in the rGOA/BN/PBO composite. These observations confirmed that the grafting of the PBO fiber improved the interfacial adhesion between the matrix and filler.

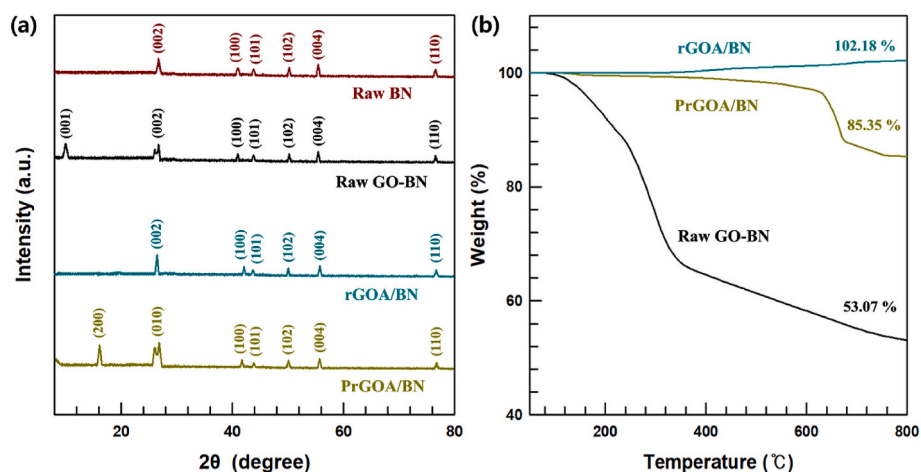


Fig. 4. (a) XRD patterns and (b) TGA graphs of fillers.

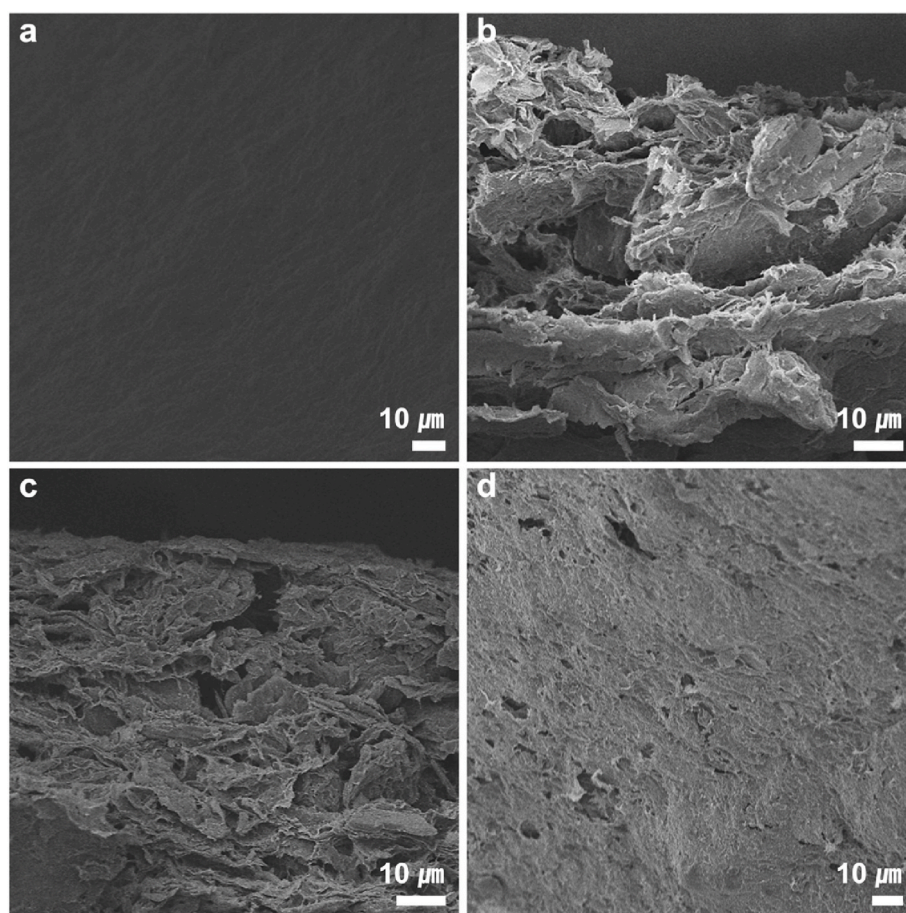


Fig. 5. FESEM images of (a) PBO matrix, (b) raw GO-BN/PBO, (c) rGOA/BN/PBO, and (d) PrGOA/BN/PBO composites.

3.4. Properties of composites

The electrical conductivities were calculated using the four-point probe method. Fig. 6(a) shows the electrical conductivity of the PrGOA/BN/PBO, and Fig. 6(b) shows the electrical conductivity of the rGOA/BN/PBO composites. The weight percentage of rGOA was fixed at 5 wt%, considering the densities of rGOA and BN. The raw GO-BN/PBO composite exhibited very low electrical conductivity values owing to low electrical conductivity of raw GO and BN. The electrical conductivities of the raw GO-BN/PBO composites are shown in Fig. S7. In this

study, rGOA was prepared by reducing GO to remove the oxygen functional groups. These defects disrupted the delocalization of the π -system with electron-withdrawing properties, so GO exhibited low electrical conductivity. With the removal of the defects after reduction, the aromaticity of the graphene sheet was recovered, and electrical conductivity was significantly improved [58]. The PrGOA/BN/PBO composites exhibited higher electrical conductivity than the rGOA/BN/PBO composites at the same filler content. With the grafting of the PBO fiber, the rGOA was evenly dispersed, thus forming an electrical conduction path more effectively. With an increase in the filler wt.% from 30 to 40,

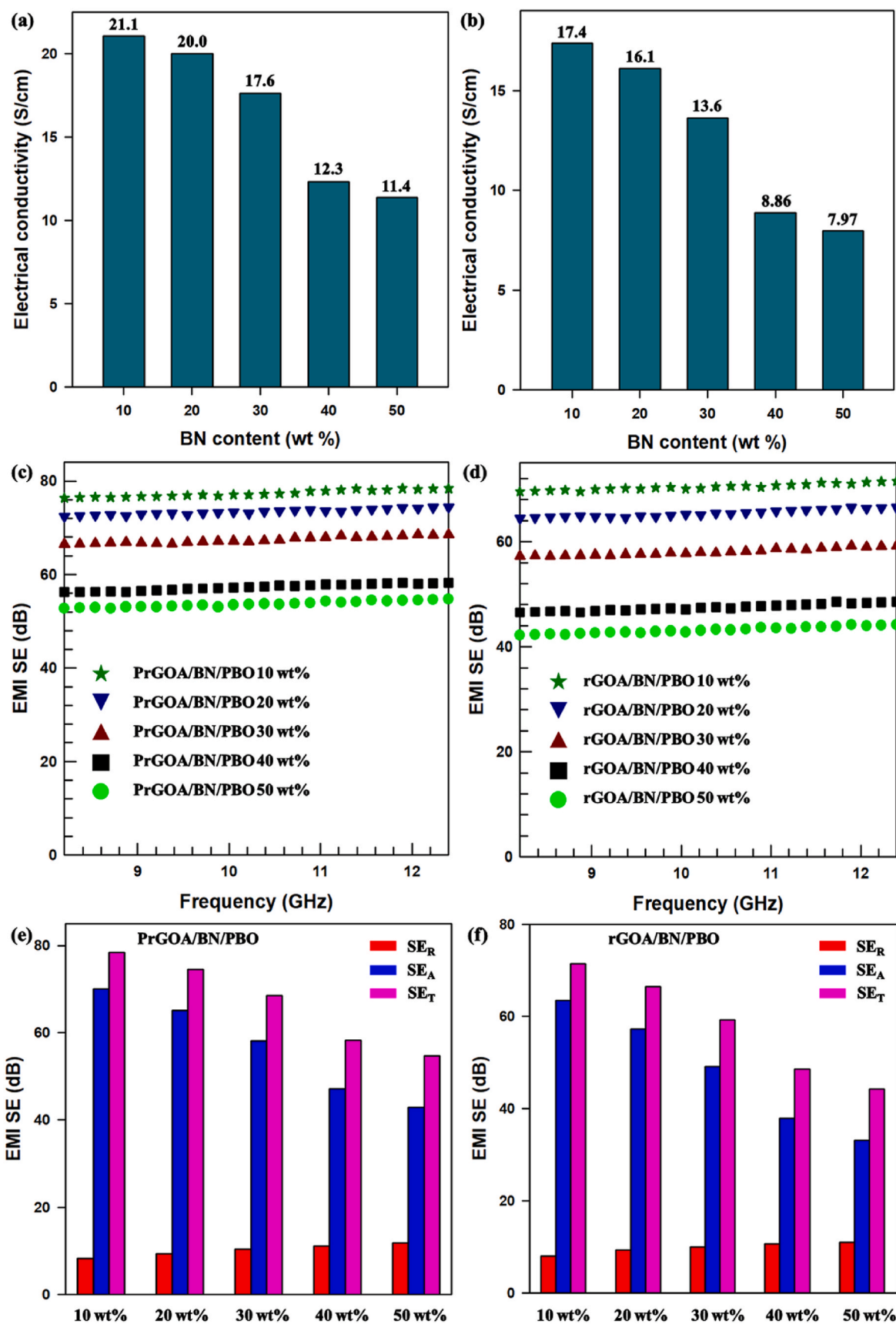


Fig. 6. (a) Electrical conductivity of PrGOA/BN/PBO and (b) rGOA/BN/PBO composites. (c) Total EMI SE values of PrGOA/BN/PBO and (d) rGOA/BN/PBO composites in the X-band (8.2–12.4 GHz). (e) SE_R, SE_A, and SE_T of PrGOA/BN/PBO and (f) rGOA/BN/PBO composites with different BN content.

the electrical conductivity decreased significantly because BNNSs completely filled the pores of rGOA and blocked the electrical conduction path. The electrical conductivity decreased as the wt.% of BN increased. The reduction in the electrical conductivity of the PrGOA/BN/PBO composite was lesser than that of the rGOA/BN/PBO composite with an increase in the filler wt.% from 30 to 40%. The PrGOA/BN/PBO composite exhibited a more uniform pore distribution, so more BNNSs are needed to entirely fill the pores of rGOA. The PrGOA/BN/PBO and rGOA/BN/PBO composites exhibited high overall electrical conductivity owing to the electrically conductive rGOA. The electrical conductivity and resistivity values of the composites are listed in Table S1.

Fig. 6(c) and (d) show the total EMI SE values of the PrGOA/BN/PBO and rGOA/BN/PBO composites in the range of 8.2–12.4 GHz (X-band), respectively. Owing to the superior electrical conductivity, the composites exhibited high EMI SE values. Electrically conductive continuous pathways of rGOA weaken EM waves by inducing ohmic loss. Charge carriers of rGOA generated current, resulting in ohmic loss and the attenuation of intensity of EM waves. Similar to the electrical conductivity, the EMI SE decreased as the filler content increased. The largest reduction in the EMI SE was observed with an increase in the weight percentage from 30 to 40. This is because the electrical conduction paths of rGOA weakened the transmitted EM waves by reflecting or absorbing the incident EM waves, but the electrical insulation property of BN deteriorated the EMI SE with an increase in the BN content. The PrGOA/BN/PBO composite exhibited enhanced EMI SE performance than rGOA/BN/PBO because of the more even dispersion of rGOA and less empty space. The possibility of the contact of the filler with the incoming EM waves increased with an increase in the density of the filler. Owing to the high electrical conductivity, large surface area, and 3D porous structure of rGOA, all the composites exhibited high EMI SE values. The 3D porous structure was effective in repeating the reflection–absorption–re-reflection process of incident EM waves [59]. Fig. 6(e) and (f) are graphs showing the reflection SE (SE_R), absorption SE (SE_A), and total SE (SE_T) values of PrGOA/BN/PBO and rGOA/BN/PBO composites, respectively. The SE_R , SE_A , and SE_T values of the composites are shown in Table S2. The high SE_A values can be attributed to the conversion of EM waves into thermal energy and the porous structure of the composites [60]. As the electrical conductivity decreased with an increase in the BN content, the SE_R value also tended to decrease. Particularly, with an increase in the weight percentage of the BN from 30 to 40%, the electrical conductivity was significantly reduced, so the reflection performance for EM waves was reduced significantly. This can be confirmed through the tendency of the SE_R values in Fig. 6(e and f). As the content of BN increased, the reflection

and multiple reflections of composites decreased, and the proportion of SE_A increased.

Fig. 7 describes the mechanism of preventing EM waves, which are incident to the composite [61,62]. EM waves are attenuated in composites through three mechanisms: reflection loss (SE_R), absorption loss (SE_A), and multiple reflection loss (SE_M). Reflection loss occurs due to surface reflection, absorption loss occurs within the material, and multiple reflection loss occurs when the EM waves penetrate the material. The total EMI SE (SE_T) is expressed by the following equation:

$$SE_T = SE_R + SE_A + SE_M$$

Electrical conductivity affects both reflection loss and absorption loss, thereby influencing EMI SE. As electrical conductivity increases, impedance mismatch increases, leading to higher reflection loss. With an increase in electrical conductivity, absorption loss also increases. This is due to the increased electromagnetic induction of currents generated within the material. The high electrical conductivity of rGOA causes large reflection loss, resulting in the first reflection. EM waves pass through the pores of rGOA and encounter interfaces. Impedance mismatch with interfaces leads to the occurrence of reflection and refraction, resulting in more multiple reflections. With the increase in multiple reflections within the pores of rGOA, the propagation path becomes longer. This results in an increase in absorption loss. Owing to the 3D porous structure of rGOA, multiple reflections and absorption occurred inside the composite. EMI SE values of composites when using non-porous rGO are listed in Table S3. The performance of composites containing rGO sheets instead of rGOA exhibited an average decrease of 53% in EMI SE. This confirmed the importance of the 3D porous structure in EMI SE performance. The composites included non-porous rGO with grafted PBO fibers also showed higher EMI SE than non-grafted composites, confirming the positive impact of grafting. The BN, with electrical insulation properties, caused a decrease in the EMI SE values while blocking the electrical conduction path. BN reduces reflections, resulting in lower reflection loss. BN hinders the contact between rGOA's surface and EM waves. As a result, multiple reflection loss and absorption loss were reduced. Therefore, EMI SE was the poorest when the BN content was the highest. In the case of rGOA/BN/PBO and PrGOA/BN/PBO composites, multiple reflection and absorption processes were repeated within the composites. Finally, the energy of EM waves was weakened and very few EM waves were transmitted.

Table 1 shows the measurement results of the flame retardancy of composites. The images of the samples exposed to flames are shown in Fig. S8. Owing to the excellent flame retardancy of the PBO used as the matrix, all the composites exhibited excellent flame retardancy. In addition, the superior flame retardancy and fire resistance of BN

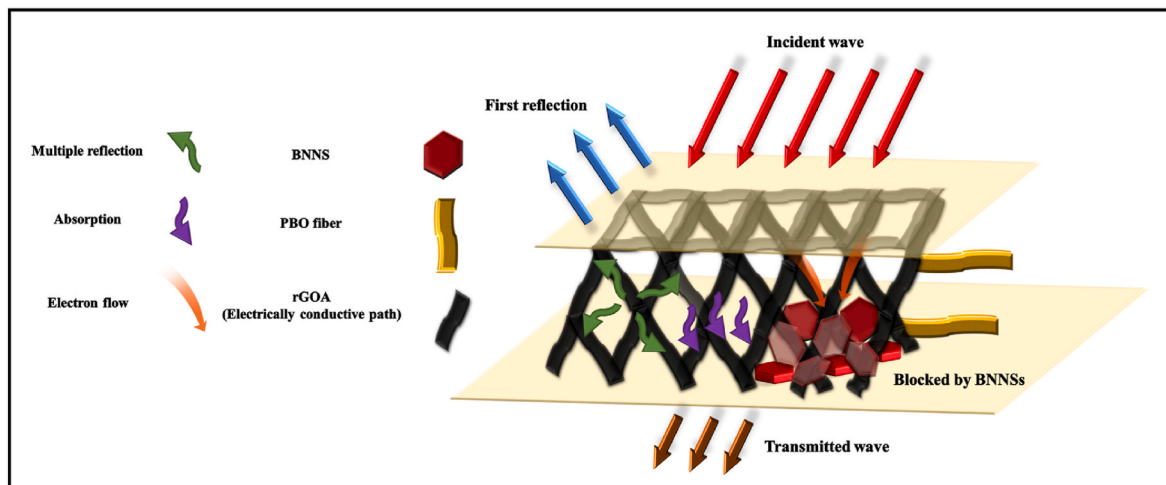


Fig. 7. EM waves shielding mechanism of PrGOA/BN/PBO composite.

Table 1
Flame resistance properties of the composite.

Samples	UL – 94V Rating	Dripping	Ignition	LOI (%)
PBO matrix	V-0	No	Yes	55.3
Raw GO-BN/PBO	V-0	No	No	58.6
rGOA/BN/PBO	V-0	No	No	66.7
PrGOA/BN/PBO	V-0	No	No	71.2

improved the flame retardancy of all the composites [52]. Owing to this effect, raw GO-BN/PBO composite also exhibited excellent flame retardancy. During the UL-94 V test, no open flame was observed in all the composites, and they were all rated V-0. The PBO matrix ignited for approximately 1 s and then was extinguished. The flame retardancy of the composites cannot be compared using only the UL-94 V test, so the limiting oxygen index (LOI) values of the composites were measured and compared. Among the composites, raw GO-BN/PBO exhibited the lowest LOI value, but it was an excellent LOI value. The rGOA/BN/PBO composite exhibited significantly improved LOI values owing to the outstanding flame resistance, self-extinguishing behavior, and thermal stability of rGOA. The high flame resistance of rGOA can be attributed to the inhibition of the formation of carbonyl defects upon exposure to flames and the holding of the non-flammable carbon dioxide gas in pores. The excellent flame resistance of PBO and BN and the self-extinguishing property of rGOA resulted in non-ignition and non-dripping properties. The LOI value increased after grafting the PBO fiber owing to the further improvement in the flame resistance by the PBO fiber. This can be attributed to the conversion of PBO fiber to char, thus generating a barrier effect [63]. Further, it can also be attributed to the high thermal stability and char yield of PBO. Fig. 8 shows the scheme of the flame-retardant mechanism of the composites.

Fig. 9(a) shows the graph obtained by plotting the thermal conductivities according to the BN content. The thermal conductivity of all the composites enhanced as the BN content increased. The thermal conductivities of the composites can be found in Table S4. The raw GO-BN/PBO composite exhibited the lowest thermal conductivity compared to other composites because of the random dispersion of the filler. This indicates the poor interfacial compatibility between hydrophilic GO and hydrophobic BN. In addition, the agglomeration of BNNSs and low thermal conductivity of raw GO contributed to the low thermal conductivity of raw GO-BN/PBO composite. The BNNSs were dispersed in the rGOA/BN/PBO composite as they were inserted into the pores of rGOA. The removal of defects on the surface of rGOA after reduction also contributed to the thermal conductivity improvement. The electrons of

rGOA contributed to heat transfer with phonons, and phonon scattering weakened as the defects decreased. The PrGOA/BN/PBO composite exhibited the highest thermal conductivity, which can be attributed to the improved interfacial adhesion between the filler and matrix after grafting the PBO fiber. The PBO fiber grafted on the rGOA/BN also formed a heat transfer path. As rGOA was more evenly dispersed, the distribution of the pores also improved, thus improving the dispersibility of BNNSs. The most significant improvement was observed at a BN weight percentage of 30% owing to the construction of a heat transfer path. This indicated the existence of a percolation threshold at approximately 30%. As the BN content increased, more numbers of BNNSs overlapped, and the heat transfer path increased. Fig. 9(b) shows a graph comparing the experimentally and theoretically obtained thermal conductivity values. The thermal conductivities theoretically calculated using the Agari-Uno model were consistent with the experimentally obtained values. Details of the Agari-Uno modeling are presented in the extended discussion of the supplementary information. Fig. 9(c) shows the scheme of the heat transport mechanism of the composite. The pores of the 3D porous structure of rGOA were filled with BNNSs. These BNNSs were connected to each other to form a heat transfer path. The grafted PBO fibers created another heat transfer path by connecting the PBO matrix and the filler. Owing to the 3D filler network structure and PBO fiber grafting, the PrGOA/BN/PBO composite exhibited the highest thermal conductivity of up to 4.81 W/m·K.

Fig. 10(a) shows the stress-strain curve of the PrGOA/BN/PBO composites according to the BN content. In the PBO matrix, the tensile strength and elongation at break were 174.7 MPa and 7.86%, respectively. The composite containing 10 wt% of BN exhibited the highest mechanical properties, with tensile strength and elongation at break of 201.84 MPa and 7.38%. After the loading of BN, the elongation at break was slightly reduced compared to that of the PBO matrix. With an increase in the BN content beyond 20 wt%, both the tensile strength and elongation at break tended to decrease. With an increase in the content from 30 to 50%, the elongation at break decreased rapidly because of the brittle nature of BN. As BN was added, additional interfaces were formed, thus generating stress concentration points. Therefore, the stress transfer of the composites did not occur uniformly, and mechanical performance was reduced. In addition, an increase in the BNNSs content resulted in the restriction of the movement of polymer chains, thus deteriorating the mechanical properties. Fig. 10(b) exhibits the comparison of the tensile strength of the composites at a fixed filler content of 10%. The raw GO-BN/PBO exhibited the lowest tensile strength owing to the low compatibility of GO and BN. This can be

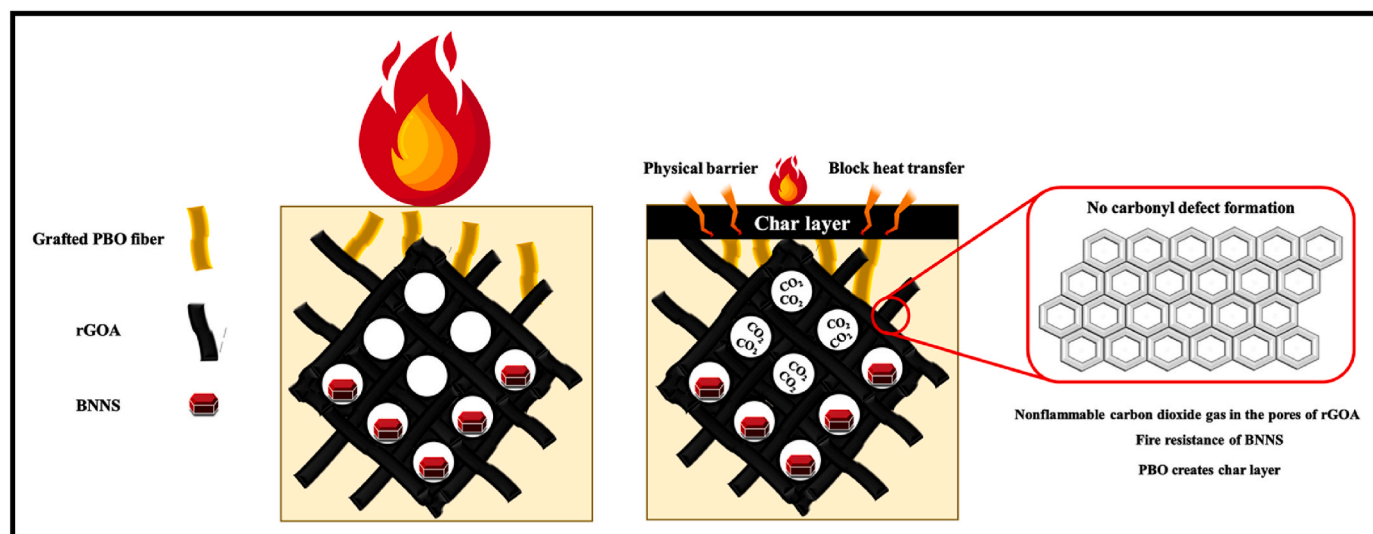


Fig. 8. Flame resistance mechanism of PrGOA/BN/PBO composite.

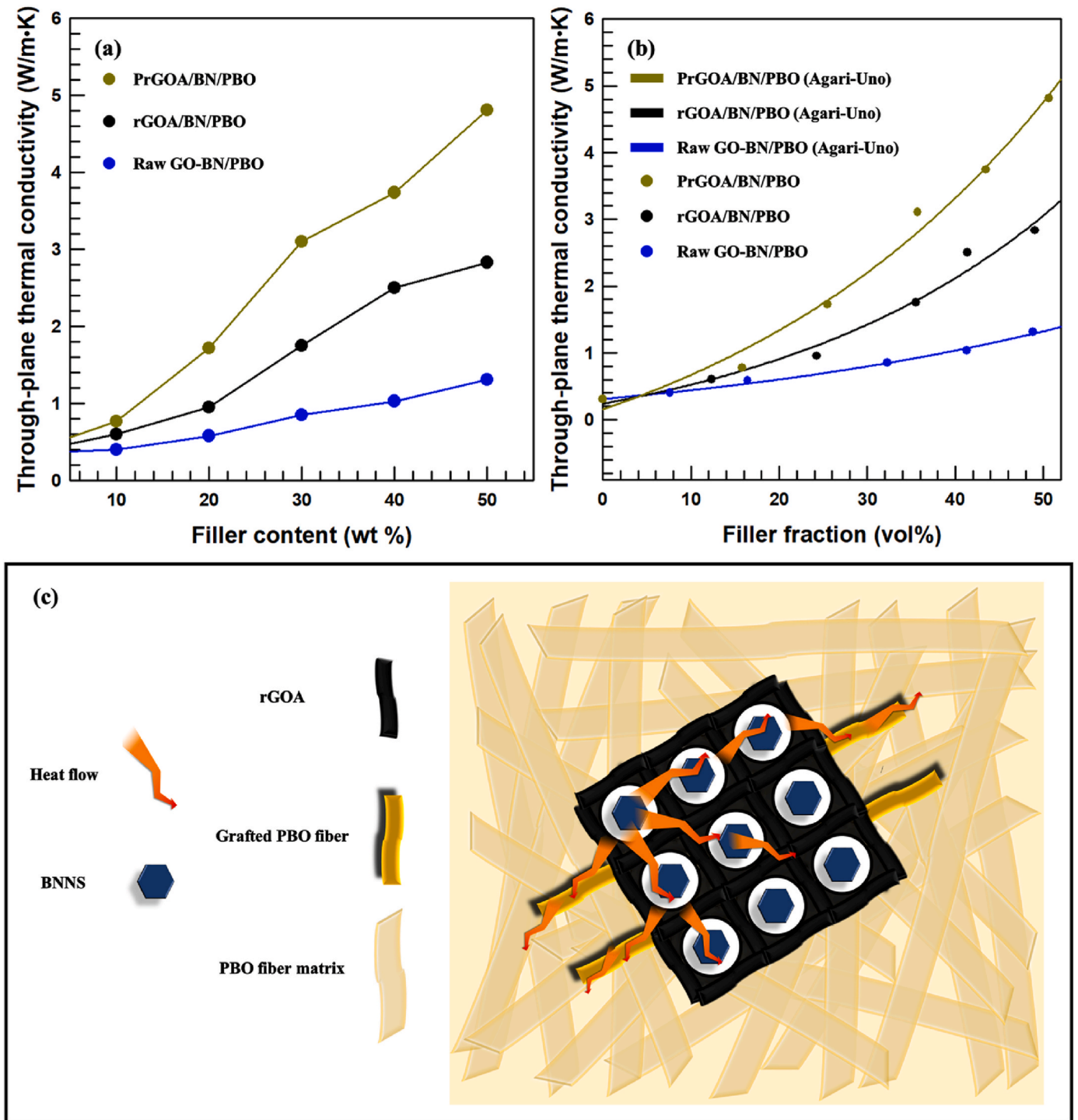


Fig. 9. (a) Thermal conductivity of composites. (b) Comparison of thermal conductivity with Agari-Uno model. (c) Heat transfer mechanism of PrGOA/BN/PBO composite.

attributed to the ineffective transfer of the stress owing to the uneven dispersion of the filler. As agglomeration occurred, the stress concentration points were generated. Nevertheless, owing to the excellent mechanical properties of PBO, raw GO-BN/PBO exhibited high tensile strength. The rGOA/BN/PBO exhibited increased tensile strength owing to the improved interfacial compatibility of rGOA and BN. The pores of rGOA prevented the agglomeration of BNNSs, thus inhibiting the formation of stress concentration points. The PrGOA/BN/PBO composite exhibited the highest tensile strength owing to the significantly improved interfacial adhesion by the grafted PBO fiber. The PBO fibers

grafted on the filler effectively delivered stress to the matrix. Fig. 10(c) shows the graph of Young's modulus of PrGOA/BN/PBO at different weight percentages of filler. The PrGOA/BN/PBO exhibited the highest value at 10 wt%, and there was no significant difference in Young's moduli values at 20 and 30 wt%. This is because the brittleness increased as the amount of BN increased, resulting in a significant decrease in both the stress and strain. At 40 and 50 wt%, Young's modulus was reduced owing to a decrease in the tensile strength. It was confirmed that the stiffness of the composite decreased as the BN content increased. Fig. 10(d) shows the comparison of Young's modulus of the

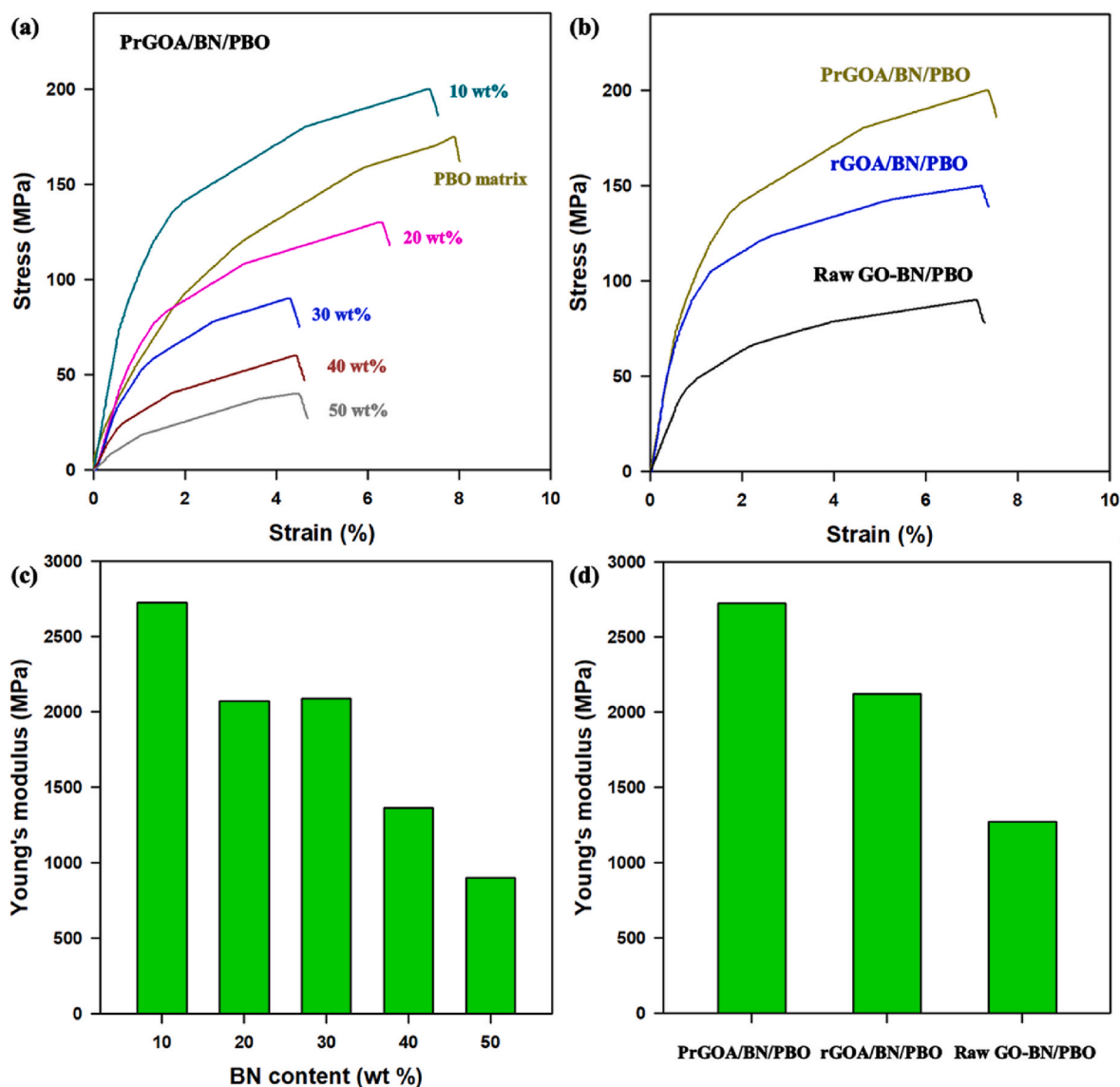


Fig. 10. (a) Stress-strain curve of PrGOA/BN/PBO composites. (b) Comparison of tensile strength of composites. (c) Young's modulus of PrGOA/BN/PBO composites. (d) Comparison of Young's modulus of composites.

composites when the BN content was 10 wt%. At a constant BN content, there was no remarkable difference in the elongation at break and brittleness. However, the difference in tensile strength was largely owing to the large difference in the interfacial bonding strength. The Young's modulus value increased with an enhancement in the interfacial compatibility, indicating that the PrGOA/BN/PBO composite exhibited the highest stiffness. Detailed information about the mechanical properties is covered in [Tables S5 and S6](#). We calculated the tensile strength and elongation at break by averaging the measurements from the five tests.

4. Conclusion

This study fabricated polymer composites with heat dissipation and EMI SE performances. To solve the low thermal and electrical conductivity of polymers, rGOA and BN fillers were introduced to the polymer. Materials used in electrical industries should exhibit flame retardancy and proper mechanical properties. In this study, PBO was used as the polymer matrix, and excellent flame retardancy and mechanical properties were obtained using the rGOA/BN hybrid filler. However, if the matrix and filler are simply mixed, the performance of the composite

decreased owing to the low interfacial compatibility. To solve this problem, GO was converted to rGOA through hydrothermal, freeze drying, and reduction processes. The removal of the oxygen functional groups on the surface improved the compatibility between rGOA and BN. Additionally, BNNSs entered into the rGOA pores, thus inducing the dispersion effect of BNNSs. The PBO fiber used in the matrix was grafted onto the rGOA/BN filler (PrGOA/BN) to significantly improve interfacial compatibility. The prepared composites exhibited superior performance owing to the significantly improved interfacial adhesion. In addition, owing to the synergetic effects between the fillers and the matrix, the composites exhibited high thermal and electrical conductivity, excellent flame retardancy, and mechanical properties. Because of these characteristics, it is expected that the composites fabricated in this study can be used in integrated, high-power, and miniaturized electronic devices.

Author statement

Jihoon Kim: Conceptualization, Investigation, Data curation, Formal analysis, Methodology, Software, Visualization, Roles/Writing – original draft, Writing-review & editing.

Jooheon Kim: Funding acquisition, Project administration, Resources, Supervision, Validation.

Declaration of competing interest

The authors declare that they have no known competing financial interests or personal relationships that could have appeared to influence the work reported in this paper.

Data availability

The data that has been used is confidential.

Acknowledgements

This work was supported by the Chung-Ang University Graduate Research Scholarship in 2023 and also supported by the National Research Foundation of Korea (NRF) grant funded by the Korea government (MSIT) (NRF-2022M3H4A1A02076956).

Appendix A. Supplementary data

Supplementary data to this article can be found online at <https://doi.org/10.1016/j.polymertesting.2023.108282>.

References

- [1] W. Huang, R.G. Askin, Reliability analysis of electronic devices with multiple competing failure modes involving performance aging degradation, *Qual. Reliab. Eng. Int.* 19 (2003) 241–254, <https://doi.org/10.1002/qre.524>.
- [2] C.W. Park, S.K. Kang, H.L. Hernandez, J.A. Kaitz, D.S. Wie, J. Shin, O.P. Lee, N. R. Sottos, J.S. Moore, J.A. Rogers, S.R. White, Thermally triggered degradation of transient electronic devices, *Adv. Mater.* 27 (2015) 3783–3788, <https://doi.org/10.1002/adma.201501180>.
- [3] L. Sang, Diamond as the heat spreader for the thermal dissipation of GaN-based electronic devices, *Functional Diamond* 1 (2021) 174–188, <https://doi.org/10.1080/26941112.2021.1980356>.
- [4] W. Zhang, Q.Q. Kong, Z. Tao, J. Wei, L. Xie, X. Cui, C.M. Chen, 3D thermally cross-linked graphene aerogel-enhanced silicone rubber elastomer as thermal interface material, *Adv. Mater. Interfac.* 6 (2019), <https://doi.org/10.1002/admi.201900147>.
- [5] W. Dai, L. Lv, J. Lu, H. Hou, Q. Yan, F.E. Alam, Y. Li, X. Zeng, J. Yu, Q. Wei, X. Xu, J. Wu, N. Jiang, S. Du, R. Sun, J. Xu, C.P. Wong, C. Te Lin, A paper-like inorganic thermal interface material composed of hierarchically structured graphene/silicon carbide nanorods, *ACS Nano* 13 (2019) 1547–1554, <https://doi.org/10.1021/acsnano.8b07337>.
- [6] Y. Zhang, Y. Yan, J. Guo, T. Lu, J. Liu, J. Zhou, X. Xu, Superior Thermal Dissipation in Graphene Electronic Device through Novel Heat Path by Electron-Phonon Coupling, *ES Energy & Environment*, 2020, <https://doi.org/10.30919/esee8c386>.
- [7] P. Tao, W. Shang, C. Song, Q. Shen, F. Zhang, Z. Luo, N. Yi, D. Zhang, T. Deng, Bioinspired engineering of thermal materials, *Adv. Mater.* 27 (2015) 428–463, <https://doi.org/10.1002/adma.201401449>.
- [8] M.A. Poothanari, J. Abraham, N. Kalarikkal, S. Thomas, Excellent electromagnetic interference shielding and high electrical conductivity of compatibilized polycarbonate/polypropylene carbon nanotube blend nanocomposites, *Ind. Eng. Chem. Res.* 57 (2018) 4287–4297, <https://doi.org/10.1021/acs.iecr.7b05406>.
- [9] J. Abraham, M. Arif P, P. Xavier, S. Bose, S.C. George, N. Kalarikkal, S. Thomas, Investigation into dielectric behaviour and electromagnetic interference shielding effectiveness of conducting styrene butadiene rubber composites containing ionic liquid modified MWCNT, *Polymer* 112 (2017) 102–115, <https://doi.org/10.1016/j.polymer.2017.01.078>.
- [10] X. Yang, Y. Guo, X. Luo, N. Zheng, T. Ma, J. Tan, C. Li, Q. Zhang, J. Gu, Self-healing, recoverable epoxy elastomers and their composites with desirable thermal conductivities by incorporating BN fillers via in-situ polymerization, *Compos. Sci. Technol.* 164 (2018) 59–64, <https://doi.org/10.1016/j.compscitech.2018.05.038>.
- [11] X. Shen, Z. Wang, Y. Wu, X. Liu, J.K. Kim, Effect of functionalization on thermal conductivities of graphene/epoxy composites, *Carbon N Y* 108 (2016) 412–422, <https://doi.org/10.1016/j.carbon.2016.07.042>.
- [12] W. Yu, Y. Peng, L. Cao, W. Zhao, X. Liu, Free-standing laser-induced graphene films for high-performance electromagnetic interference shielding, *Carbon N Y* 183 (2021) 600–611, <https://doi.org/10.1016/j.carbon.2021.07.055>.
- [13] F. Shahzad, M. Alhabeb, C.B. Hatter, B. Anasori, S.M. Hong, C.M. Koo, Y. Gogotsi, Electromagnetic interference shielding with 2D transition metal carbides (MXenes), n.d. <https://www.science.org>.
- [14] H. Lv, Y. Guo, G. Wu, G. Ji, Y. Zhao, Z.J. Xu, Interface polarization strategy to solve electromagnetic wave interference issue, *ACS Appl. Mater. Interfaces* 9 (2017) 5660–5668, <https://doi.org/10.1021/acsami.6b16223>.
- [15] H. Fang, H. Guo, Y. Hu, Y. Ren, P.C. Hsu, S.L. Bai, In-situ grown hollow Fe₃O₄ onto graphene foam nanocomposites with high EMI shielding effectiveness and thermal conductivity, *Compos. Sci. Technol.* 188 (2020), <https://doi.org/10.1016/j.compscitech.2019.107975>.
- [16] X. Jin, J. Wang, L. Dai, X. Liu, L. Li, Y. Yang, Y. Cao, W. Wang, H. Wu, S. Guo, Flame-retardant poly(vinyl alcohol)/MXene multilayered films with outstanding electromagnetic interference shielding and thermal conductive performances, *Chem. Eng. J.* 380 (2020), <https://doi.org/10.1016/j.cej.2019.122475>.
- [17] K. Wu, Y. Xue, W. Yang, S. Chai, F. Chen, Q. Fu, Largely enhanced thermal and electrical conductivity via constructing double percolated filler network in polypropylene/expanded graphite – multi-wall carbon nanotubes ternary composites, *Compos. Sci. Technol.* 130 (2016) 28–35, <https://doi.org/10.1016/j.compscitech.2016.04.034>.
- [18] B.W. Liu, H.B. Zhao, Y.Z. Wang, Advanced flame-retardant methods for polymeric materials, *Adv. Mater.* 34 (2022), <https://doi.org/10.1002/adma.202107905>.
- [19] L. Wang, H. Qiu, C. Liang, P. Song, Y. Han, Y. Han, J. Gu, J. Kong, D. Pan, Z. Guo, Electromagnetic interference shielding MWCNT-Fe₃O₄@Ag/epoxy nanocomposites with satisfactory thermal conductivity and high thermal stability, *Carbon N Y* 141 (2019) 506–514, <https://doi.org/10.1016/j.carbon.2018.10.003>.
- [20] C. Fu, C. Yan, L. Ren, X. Zeng, G. Du, R. Sun, J. Xu, C.P. Wong, Improving thermal conductivity through welding boron nitride nanosheets onto silver nanowires via silver nanoparticles, *Compos. Sci. Technol.* 177 (2019) 118–126, <https://doi.org/10.1016/j.compscitech.2019.04.026>.
- [21] R. Turczyn, K. Krulikiewicz, A. Katunin, J. Sroka, P. Sul, Fabrication and application of electrically conducting composites for electromagnetic interference shielding of remotely piloted aircraft systems, *Compos. Struct.* 232 (2020), <https://doi.org/10.1016/j.compstruct.2019.111498>.
- [22] K. Raagulan, R. Braveenth, B.M. Kim, K.J. Lim, S.B. Lee, M. Kim, K.Y. Chai, An effective utilization of MXene and its effect on electromagnetic interference shielding: flexible, free-standing and thermally conductive composite from MXene-PAT-poly(P-aminophenol)-polyaniline co-polymer, *RSC Adv.* 10 (2020) 1613–1633, <https://doi.org/10.1039/c9ra09522e>.
- [23] L. Wang, Z. Ma, Y. Zhang, L. Chen, D. Cao, J. Gu, Polymer-based EMI shielding composites with 3D conductive networks: a mini-review, *SusMat* 1 (2021) 413–431, <https://doi.org/10.1002/sus2.21>.
- [24] J. Kim, J. Kim, Pyrolyzed cellulose/rGO aerogel composites via I2 treatment and silane surface functionalization with highly improved through-plane thermal conductivity and EMI shielding effectiveness, *J. Mater. Res. Technol.* 26 (2023) 2782–2795, <https://doi.org/10.1016/j.jmrt.2023.08.083>.
- [25] H. Zhang, Y. Wang, D. Song, L. Wang, Y. Zhang, Y. Wang, Cerium-based electrocatalysts for oxygen evolution/reduction reactions: progress and perspectives, *Nanomaterials* 13 (2023), <https://doi.org/10.3390/nano13131921>.
- [26] Q. Geng, Z. Xu, J. Wang, C. Song, Y. Wu, Y. Wang, Tailoring covalent triazine frameworks anode for superior Lithium-ion storage via thioether engineering, *Chem. Eng. J.* 469 (2023), <https://doi.org/10.1016/j.cej.2023.143941>.
- [27] Y. Cao, H. Fang, C. Guo, W. Sun, Y. Xu, Y. Wu, Y. Wang, Alkynyl boosted high-performance lithium storage and mechanism in covalent phenanthroline framework, *Angew. Chem. Int. Ed.* 62 (2023), <https://doi.org/10.1002/anie.202302143>.
- [28] X. Tang, C. Liu, H. Wang, L.P. Lv, W. Sun, Y. Wang, Pristine metal-organic frameworks for next-generation batteries, *Coord. Chem. Rev.* 494 (2023), <https://doi.org/10.1016/j.ccr.2023.215361>.
- [29] H. Yu, P. Guo, M. Qin, G. Han, L. Chen, Y. Feng, W. Feng, Highly thermally conductive polymer composite enhanced by two-level adjustable boron nitride network with leaf venation structure, *Compos. Sci. Technol.* 222 (2022), <https://doi.org/10.1016/j.compscitech.2022.109406>.
- [30] V. Guerra, C. Wan, T. McNally, Thermal conductivity of 2D nano-structured boron nitride (BN) and its composites with polymers, *Prog. Mater. Sci.* 100 (2019) 170–186, <https://doi.org/10.1016/j.pmatsci.2018.10.002>.
- [31] X. Chen, J.S.K. Lim, W. Yan, F. Guo, Y.N. Liang, H. Chen, A. Lambourne, X. Hu, Salt template assisted BN scaffold fabrication toward highly thermally conductive epoxy composites, *ACS Appl. Mater. Interfaces* 12 (2020) 16987–16996, <https://doi.org/10.1021/acami.0c04882>.
- [32] Z. Liu, J. Li, X. Liu, Novel functionalized BN nanosheets/epoxy composites with advanced thermal conductivity and mechanical properties, *ACS Appl. Mater. Interfaces* 12 (2020) 6503–6515, <https://doi.org/10.1021/acami.9b21467>.
- [33] Y. Cui, D. Bao, F. Xu, Y. Gao, X. Zhang, H. Geng, Y. Zhou, Y. Zhu, H. Wang, Fabrication of EVA connected 3D BN network for enhancing the thermal conductivity of epoxy composites, *Compos. B Eng.* 224 (2021), <https://doi.org/10.1016/j.compositesb.2021.109203>.
- [34] C. Xiao, L. Chen, Y. Tang, X. Zhang, K. Zheng, X. Tian, Three dimensional porous alumina network for polymer composites with enhanced thermal conductivity, *Compos. Part A Appl. Sci. Manuf.* 124 (2019), <https://doi.org/10.1016/j.compositesa.2019.105511>.
- [35] Z. Lule, J. Kim, Thermally conductive and highly rigid poly(lactic acid) (PLA) hybrid composite filled with surface treated alumina/nano-sized aluminum nitride, *Compos. Part A Appl. Sci. Manuf.* 124 (2019), <https://doi.org/10.1016/j.compositesa.2019.105506>.
- [36] Z. Wang, G. Meng, L. Wang, L. Tian, S. Chen, G. Wu, B. Kong, Y. Cheng, Simultaneously enhanced dielectric properties and through-plane thermal conductivity of epoxy composites with alumina and boron nitride nanosheets, *Sci. Rep.* 11 (2021), <https://doi.org/10.1038/s41598-021-81925-x>.
- [37] Y. Chen, X. Hou, M. Liao, W. Dai, Z. Wang, C. Yan, H. Li, C. Te Lin, N. Jiang, J. Yu, Constructing a “pea-pod-like” alumina-graphene binary architecture for enhancing thermal conductivity of epoxy composite, *Chem. Eng. J.* 381 (2020), <https://doi.org/10.1016/j.cej.2019.122690>.

- [38] K. Yang, W. Chen, Y. Zhao, L. Ding, B. Du, S. Zhang, W. Yang, Enhancing dielectric strength of thermally conductive epoxy composites by preventing interfacial charge accumulation using micron-sized diamond, *Compos. Sci. Technol.* 221 (2022), <https://doi.org/10.1016/j.compscitech.2021.109178>.
- [39] L. Qiu, K. Yan, Y. Feng, X. Liu, X. Zhang, Bionic hierarchical porous aluminum nitride ceramic composite phase change material with excellent heat transfer and storage performance, *Compos. Commun.* 27 (2021), <https://doi.org/10.1016/j.coco.2021.100892>.
- [40] S. Lee, D. Park, J. Kim, 3D-printed surface-modified aluminum nitride reinforced thermally conductive composites with enhanced thermal conductivity and mechanical strength, *Polym. Adv. Technol.* 33 (2022) 1291–1297, <https://doi.org/10.1002/pat.5601>.
- [41] W. Lee, J. Kim, Enhanced through-plane thermal conductivity of paper-like cellulose film with treated hybrid fillers comprising boron nitride and aluminum nitride, *Compos. Sci. Technol.* 200 (2020), <https://doi.org/10.1016/j.compscitech.2020.108424>.
- [42] Z.G. Wang, J.C. Lv, Z.L. Zheng, J.G. Du, K. Dai, J. Lei, L. Xu, J.Z. Xu, Z.M. Li, Highly thermally conductive graphene-based thermal interface materials with a bilayer structure for central processing unit cooling, *ACS Appl. Mater. Interfaces* (2021), <https://doi.org/10.1021/acsmi.1c01223>.
- [43] H. Guo, H. Zhao, H. Niu, Y. Ren, H. Fang, X. Fang, R. Lv, M. Maqbool, S. Bai, Highly thermally conductive 3D printed graphene filled polymer composites for scalable thermal management applications, *ACS Nano* 15 (2021) 6917–6928, <https://doi.org/10.1021/acsnano.0c10768>.
- [44] N. Song, D. Cao, X. Luo, Q. Wang, P. Ding, L. Shi, Highly thermally conductive polypropylene/graphene composites for thermal management, *Compos. Part A Appl. Sci. Manuf.* 135 (2020), <https://doi.org/10.1016/j.compositesa.2020.105912>.
- [45] B. Shin, S. Mondal, M. Lee, S. Kim, Y. Il Huh, C. Nah, Flexible thermoplastic polyurethane-carbon nanotube composites for electromagnetic interference shielding and thermal management, *Chem. Eng. J.* 418 (2021), <https://doi.org/10.1016/j.cej.2021.129282>.
- [46] R. Cong, C. Xu, Y. Chen, F. Ran, G. Fang, Enhanced thermal conductivity of palmitic acid/copper foam composites with carbon nanotube as thermal energy storage materials, *J. Energy Storage* 40 (2021), <https://doi.org/10.1016/j.est.2021.102783>.
- [47] H. Yu, Y. Feng, C. Chen, Z. Zhang, Y. Cai, M. Qin, W. Feng, Thermally conductive, self-healing, and elastic Polyimide@Vertically aligned carbon nanotubes composite as smart thermal interface material, *Carbon N Y* 179 (2021) 348–357, <https://doi.org/10.1016/j.carbon.2021.04.055>.
- [48] Q. Hu, X. Bai, C. Zhang, X. Zeng, Z. Huang, J. Li, J. Li, Y. Zhang, Oriented BN/Silicone rubber composite thermal interface materials with high out-of-plane thermal conductivity and flexibility, *Compos. Part A Appl. Sci. Manuf.* 152 (2022), <https://doi.org/10.1016/j.compositesa.2021.106681>.
- [49] Y. Zhang, X. Tai, J. Zhou, T. Zhai, L. Xu, C. Diao, X. Xie, C. Hou, X. Sun, X. Zhang, Z. Li, W. Du, Enhanced high-temperature thermal conductivity of the reduced graphene oxide@SiO₂ composites synthesised by liquid phase deposition, *Ceram. Int.* 48 (2022) 8481–8488, <https://doi.org/10.1016/j.ceramint.2021.12.058>.
- [50] M. Šilhavík, P. Kumar, Z.A. Zafar, R. Král, P. Zemenová, A. Falvey, P. Jiríček, J. Houdková, J. Cervenka, High-temperature fire resistance and self-extinguishing behavior of cellular graphene, *ACS Nano* 16 (2022) 19403–19411, <https://doi.org/10.1021/acsnano.2c09076>.
- [51] Y. Xie, S. Xu, Z. Xu, H. Wu, C. Deng, X. Wang, Interface-mediated extremely low thermal conductivity of graphene aerogel, *Carbon N Y* 98 (2016) 381–390, <https://doi.org/10.1016/j.carbon.2015.11.033>.
- [52] Y. Chen, H. Zhang, J. Chen, Y. Guo, P. Jiang, F. Gao, H. Bao, X. Huang, Thermally conductive but electrically insulating polybenzazole nanofiber/boron nitride nanosheets nanocomposite paper for heat dissipation of 5G base stations and transformers, *ACS Nano* 16 (2022) 14323–14333, <https://doi.org/10.1021/acsnano.2c04534>.
- [53] E. Mäder, S. Melcher, J.W. Liu, S.L. Gao, A.D. Bianchi, S. Zherlitsyn, J. Wosnitza, Adhesion of PBO fiber in epoxy composites, *J. Mater. Sci.* 42 (2007) 8047–8052, <https://doi.org/10.1007/s10853-006-1311-1>.
- [54] U.K. Fatema, Y. Gotoh, Highly adhesive metal plating on Zylon® fiber via iodine pretreatment, *Appl. Surf. Sci.* 258 (2011) 883–889, <https://doi.org/10.1016/j.apsusc.2011.09.020>.
- [55] P.J. Walsh, X. Hu, P. Cunniff, A.J. Lesser, Environmental effects on poly-p-phenylenebenzobisoxazole fibers. I. Mechanisms of degradation, *J. Appl. Polym. Sci.* 102 (2006) 3517–3525, <https://doi.org/10.1002/app.24788>.
- [56] Y.W. Li, F. Zhao, Y.J. Song, J. Li, Z. Hu, Y.D. Huang, Interfacial microstructure and properties of poly (phenylene benzobisoxazole) fiber grafted with graphene oxide via solvothermal method, *Appl. Surf. Sci.* 266 (2013) 306–312, <https://doi.org/10.1016/j.apsusc.2012.12.016>.
- [57] X. Hao, J. Zhu, X. Jiang, H. Wu, J. Qiao, W. Sun, Z. Wang, K. Sun, Ultrastrong polyoxazole nanofiber membranes for dendrite-proof and heat-resistant battery separators, *Nano Lett.* 16 (2016) 2981–2987, <https://doi.org/10.1021/acs.nanolett.5b05133>.
- [58] V.B. Mohan, K. Jayaraman, M. Stamm, D. Bhattacharyya, Physical and chemical mechanisms affecting electrical conductivity in reduced graphene oxide films, *Thin Solid Films* 616 (2016) 172–182, <https://doi.org/10.1016/j.tsf.2016.08.007>.
- [59] X. Peng, X. Meng, B. Yu, H. Chen, Z. Liu, M. Tang, Y. Zheng, Y. Sun, W. Lu, Y. Dai, Graphitized and flexible porous textile updated from waste cotton for wearable electromagnetic interference shielding, *Carbon N Y* 207 (2023) 144–153, <https://doi.org/10.1016/j.carbon.2023.02.044>.
- [60] Y. Zhang, K. Ruan, K. Zhou, J. Gu, Controlled distributed Ti₃C₂T_x hollow microspheres on thermally conductive polyimide composite films for excellent electromagnetic interference shielding, *Adv. Mater.* (2023), 2211642, <https://doi.org/10.1002/adma.202211642>.
- [61] W. Xu, X. Chen, G. Zhu, Y. Yuan, F. Pan, Preparation of Mg-6Zn-1La-0.5Zr alloy sheet with excellent mechanical properties and electromagnetic interference shielding effectiveness by extrusion plus rolling, *J. Mater. Res. Technol.* (2023), <https://doi.org/10.1016/j.jmrt.2023.09.096>.
- [62] M. Wang, X.H. Tang, J.H. Cai, H. Wu, J. Bin Shen, S.Y. Guo, Construction, mechanism and prospective of conductive polymer composites with multiple interfaces for electromagnetic interference shielding: a review, *Carbon N Y* 177 (2021) 377–402, <https://doi.org/10.1016/j.carbon.2021.02.047>.
- [63] Z. Qian, M. Yang, R. Li, D. Li, J. Zhang, Y. Xiao, C. Li, R. Yang, N. Zhao, J. Xu, Fire-resistant, ultralight, superelastic and thermally insulated polybenzazole aerogels, *J. Mater. Chem. A Mater* 6 (2018) 20769–20777, <https://doi.org/10.1039/C8TA07204C>.